

Chapter 2

Introduction and Theoretical Background

If the facts don't fit the theory, change the facts.

Albert Einstein

Abstract In this chapter the theoretical background underlying this thesis is presented to the reader. Hereby, special focus is put on interpreting and motivating theoretical considerations directly in the context of mammography. At first a description on how X-rays interact with matter alongside with the respective interaction cross sections is given, which follows considerations made by Als-Nielsen and McMorrow (Elements of modern X-ray physics, 2011, [1]) and Willmott (An introduction to synchrotron radiation: Techniques and applications, 2011, [2]). The drawn conclusions exemplify why phase-sensitive imaging techniques yield the potential to prevail conventional absorption-based methods in the field of soft-tissue assessment. Afterwards the theoretical framework for grating-based imaging utilizing X-ray Talbot interferometry is introduced. Moreover, the adjustments which are necessary to translate “idealized” grating-based imaging towards clinical implementation are outlined. Finally, this chapter concludes with a brief overview on the morphology and pathological changes of the female breast as well as the clinical diagnostics and the options of treatment associated with the latter.

2.1 Interactions of X-Rays with Matter

X-rays are electromagnetic waves with wavelengths ranging from 0.1 to 100 Å. One differentiates “hard” from “soft” X-rays, if they exceed an energy of 5–10 keV. In the case of medical imaging, hard X-rays are used to achieve a sufficient penetration of tissue. Here, X-rays can interact with the tissue, more precisely its atoms, in various ways. The impinging photon can either be scattered and/or photoelectrically absorbed. In the case of scattering, elastic processes (wavelength of the photon is preserved during interaction) are distinguished from inelastic interactions (wavelength of the photon is altered during interaction). Elastic scattering at a free, charged

particle is called Thomson scattering, while the sum of coherent scattering at bound electrons is described by the Rayleigh formalism. In a semi-classical picture this process can be understood as an incident photon accelerating an electron, which in turn emits a photon with the same wavelength, albeit of different direction of propagation. In contrast, in the case of inelastic scattering, which is termed as the Compton effect, the photon “collides” with the electron, by which energy is transferred to the electron, while the photon experiences a respective decrease in frequency.

Conventional absorption-based imaging comprises mostly contribution from inelastic processes, namely photoelectric absorption and Compton scattering (elastic Rayleigh scattering is of minor impact only), while phase-contrast formation solely relies on elastic contributions. Utilizing the phenomenological concept of the complex refractive index, adapted from the description of visible light, the aforementioned interactions, which cause wave diffraction when encountering an object, can be summarized. A more detailed description of the respective absorption and phase-shift cross sections and their dependency on X-ray energy and target material characteristics is given in the following subsections.

2.1.1 Complex Refractive Index

In the case of X-rays ($\delta \ll 1$), the complex refractive index of a medium is typically written as

$$n = \underbrace{1 - \delta}_{[\text{elastic}]} + \underbrace{i\beta}_{[\text{inelastic}]}, \quad (2.1)$$

where δ denotes the refractive index decrement, which is associated with elastic interactions between the photon and the penetrated medium, and β is the imaginary part of the refractive index, which is predominately related to the respective inelastic processes. Consider an ideal, plane wave-front Ψ_v propagating in z -direction within vacuum ($n = 1$, $\delta = 0$, $\beta = 0$), which can be written as

$$\Psi_v(\vec{r}, t) = \Psi_0 e^{i(\vec{k}\vec{r} - \omega t)} = \Psi_0 e^{i(kz - \omega t)}, \quad (2.2)$$

where $\vec{k} = (0, 0, k = \frac{2\pi}{\lambda})$ denotes the wave-vector, λ is the wavelength, ω is the angular frequency, and Ψ_0 is the wave-amplitude. When the wave-front enters a medium with complex refractive index n the wave-vector k is modified to kn , as schematically depicted in Fig. 2.1a. Therefore the modified wave can be re-written in terms of the incident wave by

$$\Psi_m(z, t) = \Psi_0 e^{i(nkz - \omega t)} = \Psi_0 e^{-i\omega t} e^{i(1-\delta)kz} e^{-\beta kz} = \Psi_v(z, t) \cdot \underbrace{e^{-i\delta kz}}_{[\text{phase-shift}]} \cdot \underbrace{e^{-\beta kz}}_{[\text{attenuation}]}. \quad (2.3)$$

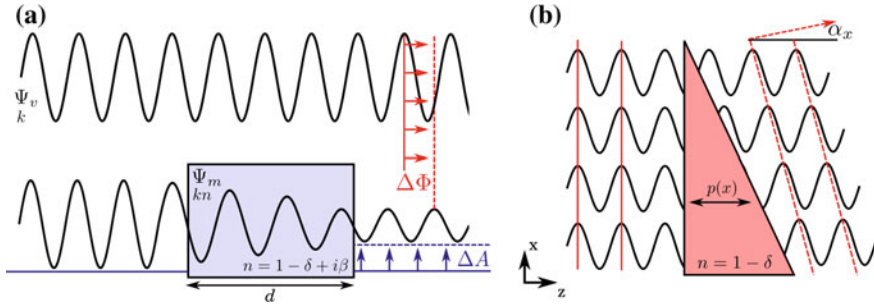


Fig. 2.1 Attenuation and phase-shift of X-rays. **a** When a wave-front Ψ_v travels through a medium with complex refractive index n , it experiences a decrease in wave-amplitude by ΔA as indicated by blue arrows, which is associated with the imaginary part of the refractive index. Further the perturbed wave Ψ_m receives a shift in the wave-phase by $\Delta\Phi$ as indicated by red arrows, which is associated with the decrement of refractive index. **b** When a wave-front travels through a phase prism ($\beta = 0$), a local variation in wave-shift implies a refraction of the wave by an angle α_x , with respect to the incident wave-front. Note that peaks of the excited waves are aligned on a line (dashed line), which is titled by the angle α_x with respect to the horizontal

Hence, after travelling through a medium with thickness d , the wave-amplitude and wave-phase of the exit-wave are modified by a factor $e^{-\beta kd}$ and $e^{-i\delta kd}$, respectively.

2.1.2 Attenuation of X-Rays

The intensity I of an electromagnetic wave is given by the square of the absolute value of its wave-function. Accordingly, the transmission value T can be calculated from the ratio of beam intensities before $I_v(z = 0)$ and after traversing a medium $I_m(z = d)$ with thickness d , using

$$T(d) = \frac{I_m(d)}{I_v(0)} = \frac{|\Psi_m(d, t)|^2}{|\Psi_v(0, t)|^2} = e^{-2k\beta d}. \quad (2.4)$$

Comparing this result to the Beer–Lambert equation

$$T(d) = \frac{I_m(d)}{I_v(0)} = e^{-\mu d}, \quad (2.5)$$

with μ denoted the linear attenuation coefficient, shows that μ equals $2k\beta$. Note that the decrease in wave-amplitude caused by a medium is given by

$$\Delta A = \Psi_v - \Psi_m = \Psi_v(1 - e^{-k\beta d}). \quad (2.6)$$

2.1.3 Phase-Shift and Refraction of X-Rays

From Eq. 2.3, we can see that a wave-front, that passes through a medium experiences a relative phase-shift $\Delta\Phi$, which equals

$$\Delta\Phi = \delta kz. \quad (2.7)$$

As a consequence thereof the perturbed wave is additionally refracted by an angle α_x with respect to the horizontal, incident wave-front. This effect becomes understandable when considering a plane of waves, that travels in z -direction through a phase prism ($\beta = 0$), as schematically depicted in Fig. 2.1b. With respect to their x -coordinate each of the waves undergoes a different phase-shift $\Delta\Phi(x)$, which is dependent on the actual optical path length of the prism $p(x)$, and given by

$$\Delta\Phi(x) = k\delta p(x). \quad (2.8)$$

From Fig. 2.1b, we can see that the phase-shifted waves have their peaks mutually aligned on a line, that is tilted by α_x with respect to the horizontal. Hence, the exciting wave-front can be considered as an array of in-phase waves with altered direction of propagation. Using geometrical considerations and small-angle approximation, the refraction angle α_x can be directly associated with the induced phase-shift, more precisely its first derivative, by [3]

$$\alpha_x \approx \sin(\alpha_x) = \frac{1}{k} \frac{\partial\Phi(x, y)}{\partial x}. \quad (2.9)$$

In the more general case of three-dimensional objects, where material entities change throughout the object, the aforementioned equations have to be extended by an integral in propagation direction, i.e.

$$T(x, y) = e^{-2k \int \beta(x, y, z) dz}, \quad (2.10)$$

$$\Delta\Phi(x, y) = k \int \delta(x, y, z) dz, \quad (2.11)$$

and

$$\alpha_x(x, y) = \frac{1}{k} \frac{\partial\Phi(x, y)}{\partial x} = \frac{\partial}{\partial x} \int \delta(x, y, z) dz. \quad (2.12)$$

In the following, we estimate typical refraction angles of X-rays in the case of soft-tissue. Consider a wave in medium (n_m), that is impinging on the interface between the medium and vacuum (n_v) at an incident angle γ_{in} (with respect to the interface orthogonal); after refraction the exit-wave exhibits an angle γ_{ex} (with respect to the interface orthogonal), that is determined by Snell's law as

$$n_m \sin(\gamma_{in}) = n_v \sin(\gamma_{ex}). \quad (2.13)$$

Assuming that the reflections are of minor magnitude only, which is justified by the fact that δ is much smaller than unity and defining the refraction angle α as difference between the exit (γ_{ex}) and the incident angle (γ_{in}), shows that α is given as

$$n_m \gamma_{in} = \gamma_{ex} = \alpha + \gamma_{in}, \quad (2.14)$$

$$\alpha = \gamma_{in}(n_m - 1) = -\gamma_{in}\delta. \quad (2.15)$$

Since α is negative, γ_{in} is larger than γ_{ex} , which implies a refraction of the wave towards the surface orthogonal. For energies typically used for phase-contrast mammography, i.e. ≤ 40 keV, δ ranges in the order of 10^{-7} – 10^{-5} (Fig. 2.2b), which accounts for refraction angles being in the regime of micro-degrees/nano-radians. Hence, to directly resolve X-ray refractions, either a long propagation distance or detectors with ultra-small pixel pitch are required, both being incompatible with clinical requirements. More advanced methods, which utilize optical elements to indirectly retrieve the phase information, are explained in Sect. 2.2.

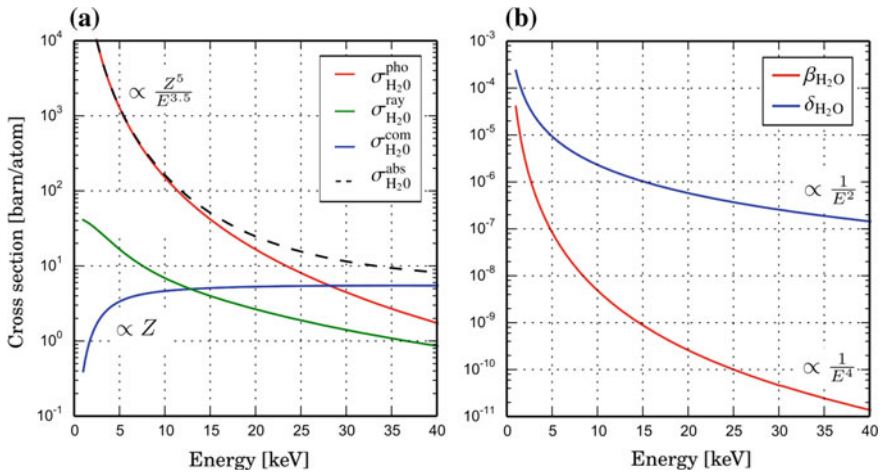


Fig. 2.2 Absorption and phase-shift characteristics of water at clinical X-ray energies. **a** Contributions to the total absorption cross section of water $\sigma_{\text{H}_2\text{O}}^{\text{abs}}$, as indicated by dashed line. Up to an energy of 30 keV the photoelectric absorption ($\sigma_{\text{H}_2\text{O}}^{\text{pho}}$) is the prevailing interaction between photons and water atoms. In the case of higher X-ray energies, the Compton effect ($\sigma_{\text{H}_2\text{O}}^{\text{com}}$) is the dominating interaction. Rayleigh scattering ($\sigma_{\text{H}_2\text{O}}^{\text{ray}}$) is hardly contributing to the absorption cross section, albeit is the prominent interaction for the generation of the phase-shift. **b** Decrement δ and imaginary part β of the refractive index of water. Note that, δ exceeds β by up to four orders of magnitude. Besides, δ decreases proportionally to the square energy E^{-2} , in comparison to β which decreases proportionally to E^{-4} . Data obtained from XOP [4]

2.1.4 Absorption and Phase-Shift Cross Section

With the goal of illustrating the benefits arising from phase-contrast in comparison to attenuation-based imaging the underlying interactions of photons with matter are investigated in more detail in the following. In a semi-classical picture, the interaction of X-rays with matter can be considered as a scattering process of an incoming electric field $\varepsilon_{in}(\vec{k})$ at the charge distribution of an atom. Here, the incoming electric field $\varepsilon_{in}(\vec{k})$ forces the bound electrons of an atom to harmonically oscillate. In return, they emit an outgoing electric field, which exhibits the shape of spherical waves $\varepsilon_{out}(\vec{k}') \propto \varepsilon_{in}(\vec{k}) \frac{e^{ikR}}{R}$, more precisely determined to

$$|\varepsilon_{out}(P, \vec{k}, E, R)| = -r_e \hat{P} f(\vec{q}, E) \underbrace{|\varepsilon_{in}| \frac{e^{ikR}}{R}}_{\text{spherical wave}}. \quad (2.16)$$

Here r_e denotes the classical electron radius, \hat{P} is a factor, which accounts for the polarisation of the field, $f(\vec{q}, E)$ is the atomic scattering factor, $\vec{q} = \vec{k}' - \vec{k}$ is the scattering vector and R is the distance from the scattering event. The atomic scattering factor, which defines the interaction process, is termed to

$$f(\vec{q}, E) = f_0(\vec{q}) + f_1(E) - if_2(E), \quad (2.17)$$

where $f_0(\vec{q})$ is the energy-independent form factor, which describes scattering at free electrons and $f_1(E)$ and $if_2(E)$ are dispersions corrections, which account for energy-dependent interactions with the bound electrons of the atom, respectively. In the case of elastic scattering, which is confined to the forward direction ($\vec{q} \approx 0$), the complex refractive index n can be directly associated with the atomic scattering factor $f(\vec{q} \approx 0, E)$, utilizing

$$n(E) = 1 - \frac{r_e \lambda^2 N}{2\pi} (f_0(0) + f_1(E) - if_2(E)), \quad (2.18)$$

where N denotes the atomic number density. Further the form factor f_0 is defined as the Fourier Transform of the charge distribution $\rho(r)$. In the considered case where scatter prevails in the forward direction the Fourier Transform equals an integration in real space. And therewith corresponds to the overall number of charges incorporated by the atom, which is equivalent to the atomic number Z , since

$$f_0(\vec{q} \approx 0) = \int \rho(r) e^0 d^3r = Z. \quad (2.19)$$

Further, the real part of the dispersion coefficient f_1 can be neglected if X-ray energies are far from the absorption edges of the investigated material. This holds

true for soft-tissue, which typically comprises low Z elements only, with absorption edges being far below the X-ray energies utilized for breast imaging. Carbon, oxygen and calcium for instance show characteristic absorption edges at 0.28, 0.53 and 4.0 keV, respectively. Correspondingly, Eq. 2.18 can be simplified to

$$n(E) \approx 1 - \frac{r_e \lambda^2 N}{2\pi} (Z + 0 - i f_2(E)) = 1 - \underbrace{\frac{r_e \lambda^2 N}{2\pi} Z}_{[\delta]} + i \underbrace{\frac{r_e \lambda^2 N}{2\pi} f_2}_{[\beta]}. \quad (2.20)$$

When we compare Eq. 2.20 derived above against Eq. 2.1, introduce the atomic absorption σ^{abs} and phase-shift cross section σ^{pha} , and additionally substitute NZ with the electron density ρ_e , we see that β and δ are given by

$$\beta(Z, E) = \frac{r_e \lambda^2 N}{2\pi} f_2 = \frac{\lambda N \sigma^{\text{abs}}}{4\pi}, \quad (2.21)$$

$$\delta(Z, E) = \frac{r_e \lambda^2 \rho_r}{2\pi} = \frac{\lambda N \sigma^{\text{pha}}}{2\pi}. \quad (2.22)$$

In comparison to the phase-shift cross section, which solely relies on elastic scattering the total absorption cross section σ^{abs} comprises multiple energy-dependent contributions

$$\sigma^{\text{abs}}(Z, E) = \sigma^{\text{ray}} + \sigma^{\text{pho}} + \sigma^{\text{com}} + \sigma^{\text{pai}}, \quad (2.23)$$

where σ^{ray} is the Rayleigh scattering cross section, which denotes elastic scattering at the bound electrons of an atom. Photoelectric absorption (σ^{pho}) describes the effect of a photon being completely absorbed by an inner-shell electron. If the photon energy exceeds the electron binding energy, the atom is ionized and the respective photo-electron emitted from the atom. Compton scattering (σ^{com}) corresponds to inelastic scattering and is given as the incoherent sum of scattering at the electrons of an atom. Here, the photon collides with an electron, which accompanies an energy transfer from the photon to the recoiling electron. Contingent on the conservation of energy and momentum the photon further experiences an increase in wavelength during the scatter event. Pair production (σ^{pai}) requires photon energies above 1 MeV and hence does not play any role for soft-tissue X-ray imaging. Figure 2.2 gives an exemplary overview on the energy dependency of the various cross sections in the case of water, which is chosen as a soft-tissue representative. Up to an energy of approximately 30 keV photoelectric absorption is the dominating interaction. For X-ray energies exceeding this value, the Compton effect is on the onset of prevailing the total absorption cross section. Finally, Rayleigh scattering is only of minor impact for the generation of absorption-based imaging contrast, albeit it is the prominent interaction for the phase-shift cross section.

The photoelectric cross section itself is heavily dependent on the atomic number of the absorbing material and rapidly decays with X-ray energy. Far from absorption edges the following proportionality holds true [5]:

$$\sigma^{\text{pho}} \propto \frac{Z^5}{E^{3.5}}. \quad (2.24)$$

Note that in the case of very hard X-rays the photoelectric cross section is proportional to $Z^5 E^{-1}$. In comparison to Eq. 2.24, the phase-shift cross section is directly proportional to the atomic number and decreases only linearly with photon energy by

$$\sigma^{\text{pha}} \propto \frac{Z}{E}. \quad (2.25)$$

This distinct difference in energy dependence renders phase-sensitive techniques beneficial for soft-tissue (low Z materials) imaging applications such as mammography: one possibility to reduce the radiation dose is to increase the mean X-ray energy. While the absorption cross section is rapidly decreasing, hence a deposition of radiation dose within the breast minimized, the phase-shift cross section remains nearly unaltered. Besides, exhibiting a “beneficial” energy dependence, phase-sensitive imaging further profits from an intrinsically increased contrast generation: δ strongly exceeds the corresponding β with respect to the absolute value, e.g. in the case of water the ratio of the latter amount to up to four orders of magnitude (Fig. 2.2b).

The Compton scattering cross section σ^{com} can be obtained by multiplying the relativistic Klein–Nishina cross section with the number of interacting electrons Z and is therefore proportional to

$$\sigma^{\text{com}} \propto \frac{Z}{E + m_e} \stackrel{E \ll m_e}{\propto} Z, \quad (2.26)$$

where m_e denotes the electron rest mass [6]. Note that within the energy regime investigated here, which is well below the rest energy of an electron, the Compton σ^{com} and phase-shift cross section σ^{pha} yield both a linear dependency in Z . This circumstance is of major importance for the multi-modality of phase-sensitive imaging. In the case of low X-ray energies, absorption-based and phase-sensitive imaging yield complementary images, since probing intrinsically different contrasts. In the case of high X-ray energies, i.e. when the Compton effect prevails the total absorption cross section, this complementarity is lost in a step-wise manner, as Eq. 2.26 shows that both cross sections only rely on the electron density of the probed sample. Nevertheless, phase-sensitive imaging is still attractive at very hard X-rays, since δ is decreasing much slower than β with respect to photon energy [7].

2.2 Grating-Based Imaging

2.2.1 The Talbot Effect

In the year 1836 Henry Fox Talbot discovered that periodically absorbing structures (like gratings) produce a self-imaging phenomenon if illuminated with coherent, visible light. Hereby, the induced intensity modulations re-occur after certain propagation distances (Talbot distances) downstream of the absorber in beam direction [8]. Lord Rayleigh analytically demonstrated that the Talbot effect arises from Fresnel diffraction (near-field diffraction) and that the full Talbot distance d_T is determined by

$$d_T = \frac{\lambda}{1 - \sqrt{1 - \frac{\lambda^2}{p_1^2}}}, \quad (2.27)$$

where λ denotes the wave length of the illuminating ray and p_1 corresponds to the period of the absorbing structure [9]. In the case of X-rays, λ ranges in between 0.1 and 100 Å, and hence is much smaller than the period of gratings implied for phase-sensitive imaging, which are typically in the size of microns. Thus, the Taylor series expansion can be used to approximate the square root in Eq. 2.27, resulting in a Talbot distance of

$$d_T = \frac{\lambda}{1 - \left(1 - \frac{\lambda^2}{2p_1^2}\right)} \stackrel{\lambda \ll p_1}{\approx} \frac{2p_1^2}{\lambda}. \quad (2.28)$$

An intuitive verification of the Talbot effect can be given by calculating the propagation of a plane wave $\Psi_0(x)$, which impings on a binary grating, dependent on the propagation distance z , using the Fresnel transform

$$\Psi_z(x) = \mathcal{F}^{-1}[\hat{P}_z(k_x)\mathcal{F}[\Psi_0(x)]]. \quad (2.29)$$

Here $\hat{P}_z(k_x)$ denotes the Fresnel propagator function, which is given as

$$\hat{P}_z(k_x) = e^{ik_z} e^{-izk_x^2/2k}, \quad (2.30)$$

where k_x and k are the x -component and the norm of the wave vector, respectively [10]. Further, the Fourier transform of the periodic wave function $\mathcal{F}[\Psi_0(x)]$ can be considered as a sum of delta-functions, which are only non-zero at frequencies k_x , that are multiple integers m of the term $2\pi/p_1$. Hence we can simplify Eq. 2.29 to

$$\Psi_z(x) = \Psi_0(x)\mathcal{F}^{-1}\left[\hat{P}_z\left(k_x = \frac{2\pi m}{p_1}\right)\right]. \quad (2.31)$$

Considering the case that the propagation distance z equals one full Talbot distance d_T , the modified Fourier space propagator function of Eq. 2.31 can be re-written as

$$\hat{P}_{d_T} \left(k_x = \frac{2\pi m}{p_1} \right) = \underbrace{e^{ikd_T}}_{[\text{phase-factor}]} \underbrace{e^{-i2\pi m^2}}_{[1]}. \quad (2.32)$$

Hence $\hat{P}_{d_T}(k_x = \frac{2\pi m}{p_1})$ corresponds to a constant phase-factor only, that is independent from both k_x and m , i.e. does not alter the amplitude/intensity of the wave. Consequently the incident wave-front repeats itself with a periodicity of d_T .

Since absorption gratings reduce the photon flux by a factor of two, which is undesirable for imaging with respect to scan time and radiation dose, it is beneficial to use phase-shifting gratings. Here the wave-front is “patterned” by alternatingly shifting its phase, rather than attenuating its amplitude [11, 12]. It is important to note that, when using a phase-shifting grating, the imprinted phase modulation does not imply an immediate change in wave-amplitude, but instead is converted into an intensity modulation downstream the grating. Thereby maximal intensity modulations are found for so-called “fractional Talbot distances” [13, 14]. Here the phase grating functions as a beam-splitter, which diffracts the incoming X-ray beam into “sub-bundles” that yield diffraction orders of mostly -1 and 1 (The unperturbed wave yields the order 0 , respectively). Correspondingly, the divided beams can then re-interfere at these fractional Talbot distances d_n , which are dependent on the imprinted phase-shift by

$$d_n = \begin{cases} n \frac{p_1^2}{8\lambda} = n \frac{d_T}{16} & \text{for } \pi\text{-shift, } n = 1, 3, 5 \dots \\ n \frac{p_1^2}{2\lambda} = n \frac{d_T}{4} & \text{for } \frac{\pi}{2}\text{-shift, } n = 1, 3, 5 \dots \end{cases} \quad (2.33)$$

Contingent on Eq. 2.7 a desired phase-shift of $\Delta\Phi = \pi$ or $\Delta\Phi = \pi/2$ can be achieved by tuning the sample material and its thickness according to the respective X-ray design energy. Typically, materials with a high electron density are used, among others nickel and gold, to relax requirements with respect to the material thickness, i.e. grating height. The aforementioned interference effect can be visualized by simulating the propagation of a fully coherent wave-front after transversing a phase grating. Figure 2.3a, b show the so-called “Talbot carpet” in the case of a $\pi/2$ -shifting and π -shifting grating with a duty-cycle of 0.5 (phase-shifting material incorporates a width of $p_1/2$) up to a propagation distance of one full Talbot distance d_T , respectively. Maximum beam interference comes to existence for odd numbers of n only, as indicated by dashed lines. In the case of a $\pi/2$ -shifting grating the 1st ($n = 1$) and 3rd ($n = 3$) fractional Talbot distances are displayed. Further, the interference pattern yields a longitudinal periodicity of $d_T/4$ and a transversal periodicity p_t of p_1 . In contrast, in the case of a π -shifting grating the longitudinal and transversal periodicity are quartered and halved, respectively, and given as

$$p_t = \begin{cases} \frac{p_1}{2} & \text{for } \pi\text{-shift} \\ p_1 & \text{for } \frac{\pi}{2}\text{-shift} \end{cases} \quad (2.34)$$

Note that the displayed Talbot carpets correspond to a mono-energetic and spatially coherent wave-front. In the case of a source with limited transverse (extended source

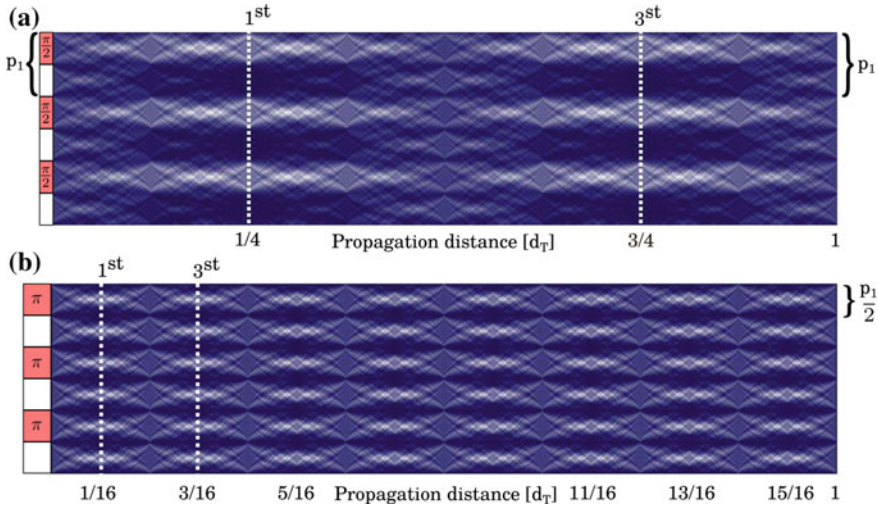


Fig. 2.3 *Talbot carpets of coherently illuminated phase-shifting gratings.* Talbot carpet generated by a $\pi/2$ -shifting (a) and π -shifting phase grating (b), yielding maximal intensity modulations at fractional Talbot distances d_n , as exemplarily indicated by *dashed lines*. Note that the period of the evoked intensity modulation p_l is halved in the case of a π -shifting phase grating. Figure adapted from Weitkamp T. et al. (2006) [13]

size) and temporal coherence (finite bandwidth), the Talbot carpet is blurred with increasing propagation distance and is given as superposition of energy-dependent contributions, respectively [15, 16].

2.2.2 X-Ray Talbot Interferometry

As calculated above (cf. Eq. 2.15), typical refraction angles induced by soft-tissue components are in the regime of micro-degrees. Hence, when using clinical detectors with pixel-sizes of hundreds of microns together with a compact setup geometry, the aforementioned refraction and small-angle scattering effects remain unnoticed. The basic idea of a Talbot grating interferometer is to track changes of the interference pattern (as described in Sect. 2.2.1) when introducing a specimen into the beam path, and relate these to the intrinsic sample properties [17]. This approach is practicable only if the interference pattern itself yields transverse intensity modulations, which are of the same order of magnitude as the evoked alternations. According to Eq. 2.34, this requirement can be fulfilled by using phase gratings with periods in the range of (sub)-microns [18].

While it is possible to directly resolve the intensity pattern with a high-resolution detector, the obtainable field-of-view is very limited, contingent on the fact that the usage of high-flux point sources is assumed [19]. In order to overcome this constraint,

i.e. to accurately sample the intensity modulations and quantify the impact of the specimen on the interference pattern with a coarsely-pixelated detector, a second so-called “analyser” grating with period p_2 , is implemented downstream the X-ray beam [20]. By moving the analyser grating perpendicular to the propagation distance over one full grating-period the intensity pattern can be sampled step-wise, which is referred to as the phase-stepping scan [21]. It is of crucial importance that the analyser grating is placed at a fractional Talbot distance d_n so that the reference pattern yields maximal intensity modulations and respective alternations of the latter can be tracked accurately. Further the analyser grating has to be matched with the transverse periodicity of the interference pattern

$$p_2 \stackrel{!}{=} p_1. \quad (2.35)$$

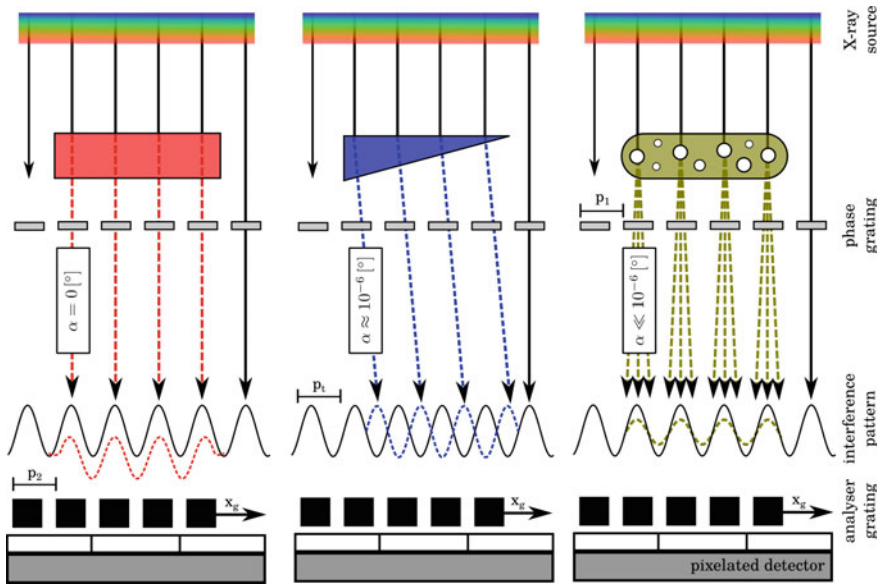


Fig. 2.4 Working principle of a Talbot grating interferometer. A phase grating creates an interference pattern with transverse intensity modulations downstream of the interferometer, arising from the Talbot self-imaging effect. When introducing a specimen the wave-front experiences local distortions, that result in changes of the intensity pattern: decrease of the overall (mean) intensity of the inference pattern, due to absorption (*red block*). Transverse shift of the interference pattern due to wave-refraction (*blue prism*). Decrease of the interference pattern amplitude, contingent on a loss of local coherence, due to diffuse, uncorrelated small-angle scattering (*green oval*). Since the evoked alternations are in (sub)-micron regime an analyser grating is implemented to precisely track the latter, if clinical detectors with a limited spatial resolution are utilized. Note that the angle α is given as a rough estimate, which is dependent on the sensitivity of the interferometer. Further the interference pattern is sine-shaped, since a X-ray generator with extended source size is assumed

Figure 2.4 gives an overview on how a specimen can alter wave-characteristics of an impinging X-ray beam, alongside with the accompanied changes introduced to the interference pattern.

Wave modifications

- Decrease of the overall (mean) intensity of the inference pattern due to absorption, as indicated by the red block.
- Transverse shift of the interference pattern, due to local refraction, as indicated by the blue phase prism.
- Decrease of the interference pattern amplitude, caused by a loss of local coherence due to small-angle scattering, as indicated by the green oval.

Note that small-angle scattering can be considered as a beam refraction process which however surpasses the sensitivity of the interferometer. In comparison to phase-shift related beam deviations, small-angle scattering yields uncorrelated, diffuse angular deflections of very small magnitude, which results in a “smearing” rather than shifting of the interference pattern, attributed to a local degradation of wave-front coherence.

2.2.3 Phase-Stepping

Within the phase-stepping scan either of the gratings is moved over one full grating period perpendicular to the beam direction and multiple images are taken at intermediate grating positions x_g . One can easily imagine that the phase-stepping curve yields minimal intensity, if the absorber grating bars superimpose the interference pattern maxima and yields a maximum, if the latter are conveniently displaced by half a grating period. To assure a meaningful sampling of the interference pattern a sufficient attenuation of the X-rays is required. Therefore the analyser grating is typically made of highly absorbing materials such as gold, with grating heights of 50–160 μm . Such microstructures can be fabricated by applying deep-etching or photolithography to a substrate layer, i.e. definition of the grating pattern, followed by a subsequent filling of the mask with the desired material via electro plating (a detailed description can be found in David C. et al. (2007) [22]).

In the case of an idealized illumination the interference pattern features an intensity modulation that is box-shaped (as sketched in Fig. 2.3). Correspondingly the phase-stepping curve yields a triangular shape if sampled (convoluted) with an analyser grating that exhibits a flat-top absorption profile. However, considering that X-ray sources have a finite source size, which can be modelled by a Gaussian distribution, the generated intensity modulations and phase-stepping curve exhibit a wave- and sine-shape, respectively. Figure 2.5 shows the respective phase-stepping curves of a blank scan (solid line), which maps the pure interference pattern and a respective sample scan (dashed line) sampling the interference pattern, which is modified

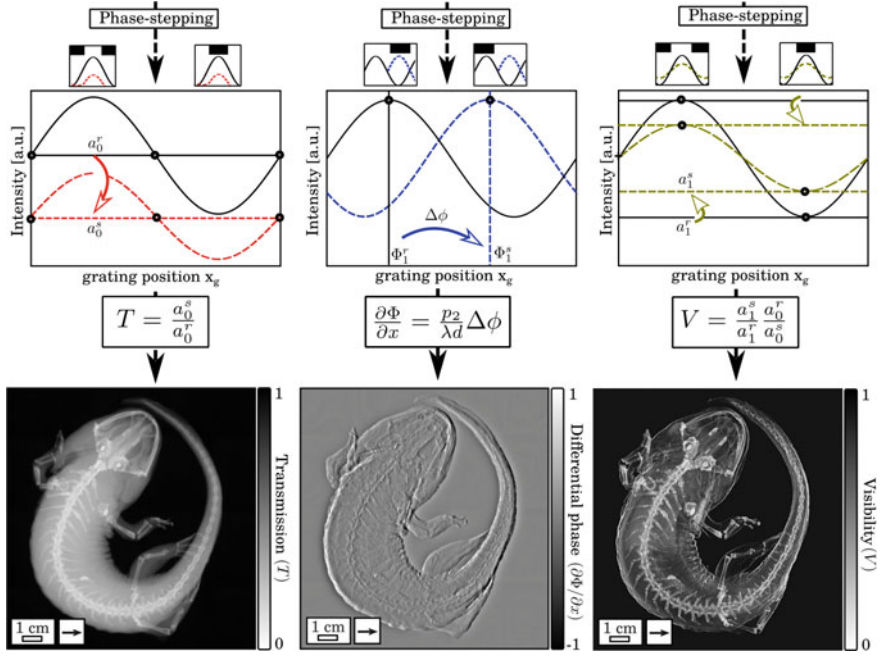


Fig. 2.5 Retrieval of the trimodal image contrast via phase-stepping. In order to precisely analyse and record the interference pattern, one of the two gratings is subsequently moved in a step-wise manner perpendicular to the alignment of the grating bars. By comparing the flat-field (*blank line*) and sample phase-stepping curve (*dashed line*) through Fourier analysis, the transmission image T , differential phase signal $\frac{\partial \Phi}{\partial x}$ and the visibility map V of the specimen can be simultaneously retrieved. Following clinical conventions the absorption and dark-field image are displayed, which are derived as transmission and visibility signal with an inverted *gray-scale*, respectively

by attenuation, refraction and small-angle scattering processes. In order to utilize grating-based imaging with clinical, large field-of-view detectors, a reference scan over the full active imaging area (flat-field) is conducted prior to measurements, in order to account for imperfections, such as Moiré Fringes (see Chap. 3) and an irregular beam illumination.

The intensity $I(x_g, x, y)$ measured during a phase-stepping scan at interlaced grating positions x_g , can be described using a Fourier-series

$$I(x_g, x, y) = \sum_{n=0}^{\infty} a_n(x, y) \cos \left(2\pi n \frac{x_g}{p_t} - \phi_n(x, y) \right), \quad (2.36)$$

where x, y denote the detector coordinates and a_n, ϕ_n are the amplitude and phase coefficients, respectively. In the case of limited beam coherence, where the projected source size s^* itself is not significantly smaller than the interference pattern period p_t , it is sufficient to consider only the first two order terms ($n \leq 1$) [23]:

$$I(x_g, x, y) \stackrel{s^* \geq \frac{p_t}{2\pi}}{=} a_0(x, y) + a_1 \cos \left(2\pi \frac{x_g}{p_t} - \phi_1(x, y) \right). \quad (2.37)$$

Here, the projected source size s^* is defined as

$$s^* = s \frac{d}{l'}, \quad (2.38)$$

where s is the source size, l' is the distance between the X-ray source (see also Sect. 2.2.5) and phase grating, and d the distance between phase and analyser grating, respectively (note that the phase grating is considered as a “sample” in this case). When using conventional X-ray sources, where the aforementioned condition $s^* \geq \frac{p_t}{2\pi}$ holds true, the phase-stepping curve is consequently of sinusoidal shape (oscillation amplitude a_1 , phase ϕ_1) additionally yielding an offset a_0 . The “quality” of the interference pattern, which is an important performance parameter of the grating interferometer, is given by how pronounced the intensity oscillation a_1 is in comparison to the mean intensity value a_0 . This parameter is associated with the so-called “flat-field visibility” V^r , i.e. normalized oscillation amplitude, by

$$V^r(x, y) = \frac{a_1(x, y)}{a_0(x, y)}. \quad (2.39)$$

From an analytic point of view at least three data points have to be acquired, for the purpose of accurately fitting the stepping curve with a sine-function. To enhance computing speed the retrieval of the phase-stepping curve is typically implemented via Fourier analysis.

2.2.4 Contrast Retrieval

Since soft-tissue samples generally attenuate, refract and scatter an incident beam at the same time, it is necessary to retrieve and separate the underlying contributions from a single phase-stepping curve. In the following the superscript (r) and (s) denote the curve parameters related to the reference (flat-field) and sample scan, respectively.

• Absorption

The transmission T through a sample is given by the relative decrease of the curve’s mean intensity, determined by the ratio of the zero-order Fourier coefficients, by

$$T(x, y) = \frac{a_0^s(x, y)}{a_0^r(x, y)}. \quad (2.40)$$

Further, following Eq. 2.6 the transmission shows an exponential behaviour and can be related to the linear attenuation coefficient μ of a sample by

$$T(x, y) = e^{-\int \mu(x, y, z) dz}. \quad (2.41)$$

Within this thesis—following clinical conventions—the absorption image A rather than transmission image is displayed and is given by

$$A(x, y) = 1 - T(x, y), \quad (2.42)$$

i.e. by inverting the gray-scale of the transmission image, strongly absorbing structures yield high image signal and are color-coded white on a non-absorbing, black background.

• Differential phase

The transverse shift S introduced to the interference pattern by a refracting sample, is given by the radian measure, hence obtained by the multiplication of the refraction angle α (small-angle approximation) and the inter-grating distance d , as

$$S(x, y) = d\alpha. \quad (2.43)$$

Accordingly, the transverse shift S is converted into a displacement of the stepping curve, namely phase position $\Delta\phi$, which is encoded by the analyser grating and dependent on its period p_2

$$\Delta\phi(x, y) = \phi_1^s(x, y) - \phi_1^r(x, y) = 2\pi \frac{S(x, y)}{p_2}. \quad (2.44)$$

In Sect. 2.1.3 we demonstrated that a variation (perpendicular to the propagation distance) in the decrement of refractive index of a specimen imposes local variations on the phase of the penetrating wave. Further these are directly proportional to the angle, by which the transmitted wave is refracted. Combination of Eqs. 2.12, 2.43 and 2.44 shows that the retrieved signal maps the differential-phase of the refracted wave and the differential, projected decrement of refractive index of the sample, by

$$\frac{\partial\Phi(x, y)}{\partial x} = k \frac{\partial}{\partial x} \int \delta(x, y, z) dz = \frac{p_2}{d\lambda} \Delta\phi(x, y). \quad (2.45)$$

• Dark-field

The local scatter power of a sample is given by the relative decrease in the normalized oscillation amplitude, hence can be calculated from the ratio of sample and reference visibility, using

$$V(x, y) = \frac{V^s(x, y)}{V^r(x, y)} = \frac{a_1^s(x, y) a_0^r(x, y)}{a_1^r(x, y) a_0^s(x, y)}. \quad (2.46)$$

In analogy to the absorption signal, the dark-field image D is obtained as

$$D(x, y) = 1 - V(x, y), \quad (2.47)$$

i.e. corresponds to the visibility map with inverted gray-scale. Strongly scattering structures yield high image signal and are color-coded white on a non-scattering, black background.

The dark-field image maps (incoherent) ultra-small and small-angle scattering of a sample incorporating high density fluctuations on the (sub)-micron scale [24]. It is of major importance that the imaging sensitivity itself is decoupled from the actual, spatial resolution of the interferometer. This so-called “sub-resolution sensitivity” hence enables the retrieval of microstructural properties of a specimen using clinically compatible pixel sizes. This circumstance is illustrated by Fig. 2.6. Here, the visibility signal is simulated for different numbers and sizes of calcium-oxalate grains on the supposition that the overall volume of calcium-oxalate is fixed [25]. While the transmission is constant for all different configurations, contingent on an unaltered amount of attenuating material, the most pronounced dark-field signal is found for calcium oxalate grains, that exhibit sizes similar to the analyser grating period p_2 . Correspondingly, grain sizes strongly exceeding p_2 , evoke scattering with diffraction angles being too small for causing sufficient loss in beam coherence. Besides, the dark-field image is found to exhibit an exponential dependence, if the angular scattering distribution is Gaussian shaped [26]. Hence, by introducing the linear diffusion coefficient ϵ —in analogy to the linear attenuation coefficient μ —the visibility signal is given by

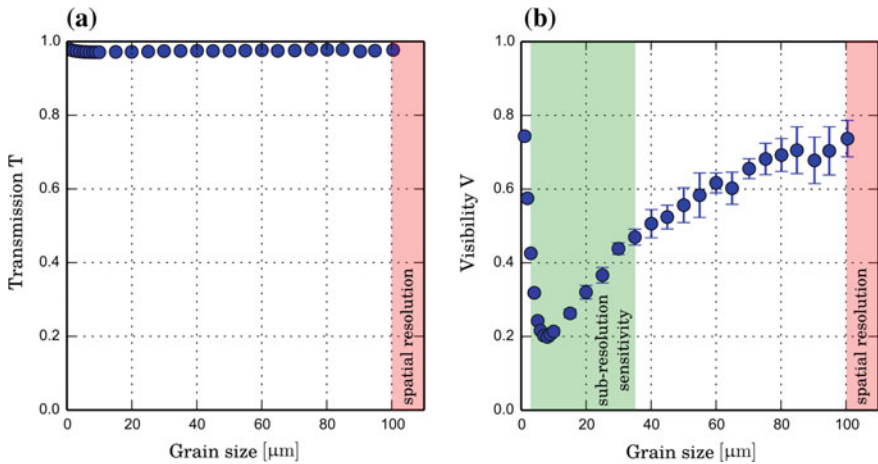


Fig. 2.6 Sub-resolution sensitivity of grating-based dark-field imaging. **a** Transmission and **b** visibility signal simulated for an assembly of calcium grains with varying grain size. The overall amount of calcium, given by the number and size of grains, is fixed for all configurations. The absorption signal is non-sensitive towards variations in the grain size. In comparison, the visibility signal yields a minimum for grains which are similar in size to the analyser grating period (green), even if strongly exceeding the spatial resolution (red) of the interferometer. Hence, dark-field imaging provides an efficiency gain in terms of spatial sensitivity by two orders of magnitude

$$V(x, y) = e^{-\frac{2\pi^2 d^2}{p_z^2} \int \epsilon(x, y, z) dz}, \quad (2.48)$$

where $\frac{2\pi^2 d^2}{p_z^2}$ corresponds to a setup-specific pre-factor. More precisely, Strobl et al. showed that the inter-grating distance, beam energy and analyser grating period determine the so-called “autocorrelation length” of the interferometer [27]. By adapting the latter the sensitivity towards certain sized scattering structures and therewith clinical applications can be tuned to a certain extent. In Chaps. 6 and 8, we utilize the circumstance that both the dark-field and absorption signal yield an exponential dependence for the quantitative (thickness-independent) retrieval of microstructural properties of microcalcifications and kidney stones, respectively. A more detailed investigation of the origin of the dark-field contrast and its dependence on sample properties can be found in Yashiro W. et al. (2010) [28].

2.2.5 Adaptations for Clinical Use

2.2.5.1 Incoherent X-Ray Sources

As stated above, the flat-field visibility V^r of a grating interferometer is an important performance parameter and is preferably tuned as high as possible. Firstly, a high visibility provides a large dynamic range for the detection of scattering until the signal saturates, i.e. the retrieval of the phase-stepping curve is only practicable if V^r is different from zero. Secondly, the photon noise of the measured differential phase scales linearly with the visibility; hence the differential-phase channel exhibits a contrast-to-noise ratio that is directly proportional to the interferometer visibility [29].

The theory presented in the last section assumed a fully coherent and parallel beam illumination, which however is not provided by compact X-ray tubes as used in clinical practice. In case of the latter an extended source size s with strongly limited transverse beam coherence is inherent, which ad-hoc prevents the Talbot interference effect to appear. A detailed theory on optical coherence can be found in Born M. et al. (1999) [30].

Transverse Coherence (Extended Source)

This is intuitively comprehensible, considering the extended source size s as an array of independent point sources as schematically depicted in Fig. 2.7a. Following Eq. 2.38, all of these create interference patterns at the analyser grating plane, which are displaced with respect to each other up to a distance equal to the projected source size s^* . If the transverse displacement between two interference patterns is non-negligible in comparison to the period of the intensity modulation p_t , the intensity oscillations are superimposed in a destructive manner, resulting in a smearing out of the combined interference pattern. More precisely, the (flat-field) visibility in case of monochromatic illumination is determined by the convolution of source size and

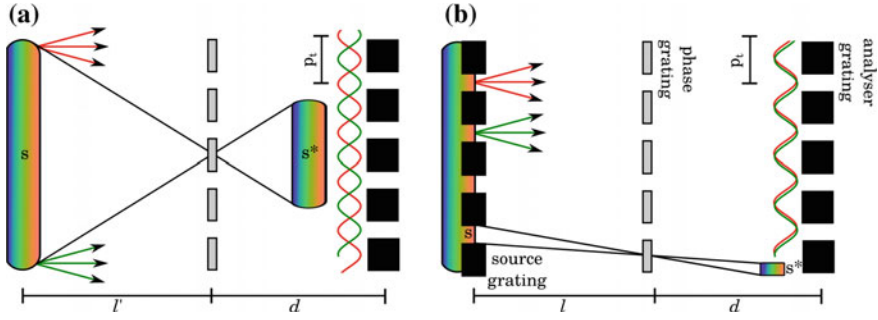


Fig. 2.7 Talbot interferometry using incoherent X-ray sources. **a** An extended sources size creates multiple interference patterns at the analyser grating plane, which are shifted against each other up to a distance of the projected source size s^* . If s^* exceeds the period of the intensity modulations p_t , the shifted patterns overlap in a destructive manner, resulting in a visibility being zero as exemplarily indicated by the *red* and *green* curve. **b** By implementing a highly absorbing source grating the extended source size is shaped into an array of fine slit sources, where each of the latter meets the coherence requirements. As a consequence, the generated intensity modulations overlap in a constructive manner as indicated by the *red* and *green* curve

interference pattern and is analytically described by [23]

$$V^r \left(\frac{s^*}{p_t} \right) = \frac{8}{\pi^2} e^{-2\pi^2 \left(\frac{s^*}{p_t} \right)^2}. \quad (2.49)$$

For projected source sizes being equal to or exceeding half the period of the interference pattern the visibility can be considered as zero, as exemplarily indicated in Fig. 2.7a. Hence to render phase-sensitive imaging with a Talbot interferometer possible, the projected source size s^* needs to be considerably small in comparison to p_t and p_2 , respectively

$$\left[s^* = s \frac{d}{l'} \right] \ll \frac{p_t}{2}. \quad (2.50)$$

This requirement is fulfilled for synchrotron beam-lines, which provide a high spatial and temporal coherence, however are space- and cost-intensive facilities. While micro-focus X-ray tubes can provide sufficiently small focal spots, they only yield little photon flux, a limited anode current and power output, and hence are only suitable for the investigation of optically thin samples. Finally, a small projected source size can also be achieved by tuning the d -over- l' ratio, for instance by increasing the distance between X-ray source and the phase grating. This however comes at the expense of extending the setup and reducing the photon flux per solid angle.

To overcome this restriction and to utilize phase-sensitive imaging within a clinical environment (compact systems, high-power sources with intrinsically large focal spots $\geq 100 \mu\text{m}$, short exposure times), a third so-called “source” grating with period p_0 is introduced just downstream the X-ray emission source, which decouples the

source size from the spatial coherence constraint [31]. Similar in design to the analyser grating, the source grating preferably exhibits a flat-top attenuation profile, by which the extended source is shaped into an array of fine slit sources. Here each slits meets the transverse coherence requirement given by Eq. 2.50. By matching the projected periodicity of the source grating p_0^* with the analyser grating period p_2

$$\left[p_0^* = p_0 \frac{d}{l} \right] \stackrel{!}{=} p_2, \quad (2.51)$$

where l denotes the distance between source and phase grating, the evoked interference modulation superimpose in a constructive manner at the detector plane as schematically shown in Fig. 2.7b. This effect is known as “Lau-effect”, which is why a three grating interferometer is referred to as a “Talbot–Lau interferometer”. Note that the effective spatial resolution of the system, i.e. sample magnification, is not altered by the presence of the gratings, but instead is determined by the projected source size, the sample position and the detector characteristics.

Temporal Coherence (Finite Bandwidth)

In comparison to the strict requirements for spatial coherence, Talbot–Lau Interferometry is compatible and successfully operated with temporally incoherent X-ray sources. However, since the phase-shift and the Talbot distances are wavelength dependent, the resulting Talbot carpet is blurred in the case of polychromatic illumination, given as a superposition of multiple, longitudinally displaced interference patterns. The visibility spectrum, which describes to what extent certain X-ray wavelengths contribute to the overall fringe visibility, thus needs to be matched to the utilized X-ray source spectrum.

To maximize the interferometer visibility the implemented gratings need to meet the following design criteria [32]:

1. The phase grating design energy must be matched to the mean X-ray energy in both the sample and flat-field scan.
2. The absorber gratings must block high energy parts of the X-ray spectrum to a sufficient extent. Note that this is of special importance in the case of integrating detectors, which give high energy photons more weight.

Since the visibility spectrum furthermore is dependent on the imprinted phase-shift as well as the Talbot-order, following considerations are essential:

3. In the case of high fractional Talbot-orders ($n > 3$) a π -shift is favourable, since the visibility spectrum yields only positive contributions. Contrasting, in the case of a $\pi/2$ -shifting grating, the evoked intensity modulations are alternating out-of-phase, resulting in a cancellation of visibility contributions.
4. In the case of low fractional Talbot-orders ($n \leq 3$) a $\pi/2$ -shift is favourable, being less sensitive to variations in the duty-cycle as in comparison to a π -shift.

2.2.5.2 Cone-Beam Geometry

Since mammography systems require a large field-of-view at a compact system length, a divergent beam is inherent and magnification effects need to be considered. Above derived equations assumed a fully parallel beam and need to be refined if the geometrical magnification of an interferometer is different from unity. In the case of cone- or fan-beam geometry the interference pattern experiences a magnification in lateral direction, which has to be matched by the analyser grating period as indicated by the superscript (M). The interference pattern magnification M is given by

$$M = \frac{d + l}{l}, \quad (2.52)$$

with d and l being the inter-grating distances as depicted in Fig. 2.7b. Following Eqs. 2.34 and 2.35, the requirements with respect to the magnified interference pattern p_t^M and adapted analyser grating period p_2^M are fulfilled, if

$$p_2^M \stackrel{!}{=} p_t^M = M p_t = \begin{cases} M \frac{p_1}{2} & \text{for } \pi\text{-shift} \\ M p_1 & \text{for } \frac{\pi}{2}\text{-shift} \end{cases} \quad (2.53)$$

holds true. Furthermore, the (fractional) Talbot distances d_n^M are increased in longitudinal direction by

$$d_n^M = M d_n. \quad (2.54)$$

Finally, contingent on Eq. 2.51 the period of the source grating needs to be adapted to

$$p_0^M \stackrel{!}{=} p_2^M \frac{l}{d}. \quad (2.55)$$

Note that a cone-beam setup exhibits further challenges which need to be addressed. The cone-beam is shadowed in the outer regions of the source and analyser grating, where grating bars are not parallel to the beam path. Correspondingly, within the affected areas the beam intensity is reduced, noise increased and the X-ray spectrum hardened, respectively. Besides, with increasing beam divergence, the effective grating profile is flattened, which results in a loss of visibility [33].

2.3 The Female Breast

2.3.1 Breast Anatomy

The female breast is a complex organ comprising, among others, mostly adipose and glandular tissue, as schematically depicted in Fig. 2.8a. Overlaying the pectoralis

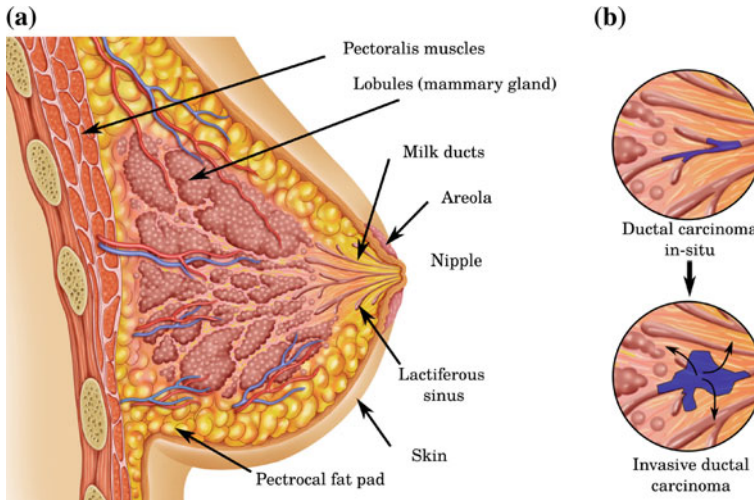


Fig. 2.8 *Anatomy of the female breast.* **a** Sketch of the female breast with mammary gland, lobules and ducts being embedded within adipose tissue. Figure adapted from Lynch, J. (2007) [36]. **b** Soft-tissue breast cancer mostly occurs within the milk ducts or within the lobules. Pre-invasive, so-called “in-situ” lesions are confined to inner compartments of the ducts, albeit bear a high risk of developing into invasive carcinomas

major muscle, the breast consists of a core of 14–18 lactiferous lobes. These are interconnected with the nipple by multiple milk ducts, which are 2–4.5 mm in diameter. Each lobe itself is composed of 20–40 terminal ductal lobular units, which are responsible for the generation of the fatty breast milk. The mammary gland is supported by a framework of connective tissue, comprising collagen, elastin and white fat. Further so-called “Cooper’s ligaments”, which are fibrous-tissue prolongations, perfuse from the muscle to the skin, maintaining the firmness and shape of the breast. The glandular tissue core is embedded in subcutaneous adipose tissue and a superficial tissue layer [34].

The (optical) density of the female breast highly varies interindividually, mainly depending on age and hormonal factors like menopausal state or external hormone replacement therapy. Usually, in the case of young women breast tissue is highly (optical) dense, contingent on a prevailing amount of glandular tissue. This circumstance and the higher sensibility of the breast towards X-rays in young women, render this group rather unsuitable for screening mammography. In postmenopausal women however, the ovarian estrogen production decreases. Since the estrogen functions as a biochemical stabilizer of glandular tissue, the latter withers and a subsequent replacement with adipose tissue occurs. Note that the fatty degeneration of elderly breasts is the decisive point in the diagnostic performance of mammography, enabling an easy detection of soft-tissue lesions in the otherwise fatty tissue. According to the American College of Radiology (ACR) four different breast density types are

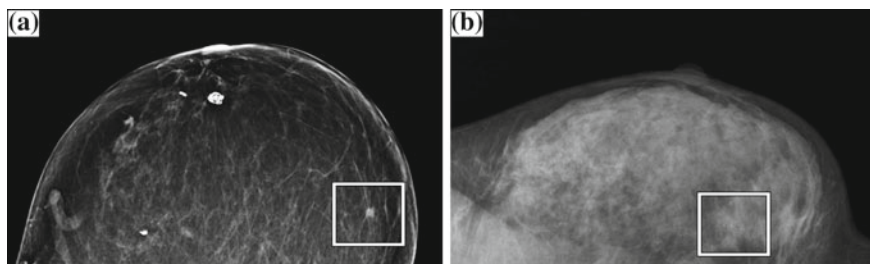


Fig. 2.9 *Mammographic appearance of ACR 1 and ACR 3 breasts. a* Clinical in-vivo mammogram of an entirely fatty breast (ACR 1) in craniocaudal (CC) view. Note that the tumor nodule (*white frame*) can be easily differentiated from the surrounding adipose tissue as a strongly absorbing spot. *b* Clinical in-vivo mammogram of a heterogeneously dense breast (ACR 3) in mediolateral oblique (MLO) view (rotated). Note that the tumorous region (*white frame*) can hardly be differentiated from the surrounding healthy tissue, being superimposed by dense breast tissue, i.e. anatomical noise

distinguished in mammographic examinations [35].

Breast density classification (ACR)

1. Fatty—The breast is considered as almost entirely adipose, i.e. the amount of glandular tissue is less than 25 %.
2. Scattered fibroglandular—The breast yields a volume of 25–50 % of well separated fibrous and glandular tissue.
3. Heterogeneously dense—The volume of breast parenchyma accounts to 51–75 %, while the breast exhibits clear features and a distinct tissue variation in the mammogram.
4. Extremely dense—Fibroglandular tissue occupies more than 75 % of the breast, which results in a homogeneous breast density and poor differentiation of features in the mammogram.

Note that an increased breast density does not only reduce the detection quality of cancer and architectural distortions resulting in a restricted diagnostic accuracy in dense breasts (cf. Fig. 2.9b), but is also associated with an increased risk of developing cancer [37].

2.3.2 Breast Cancer

Breast cancer is the most common type of invasive cancer in woman and accounted for the second most cancer deaths among woman (13.7%) in the year 2008, being of special severity in the 3rd world countries [38]. In low-income countries survival-rates are below 40 % in comparison to more than 60 % in first world coun-

tries, contingent on a lack of early detection possibilities, with an accordingly high proportion of women presenting with late-stage cancer [39]. The Global Health Estimates (WHO) assessed a number of more than half a million of breast cancer deaths in the year 2011.

Like any other cancer, malignant changes in the breast mainly occur in elderly woman as natural cell processes, where cell repair or apoptosis (process of programmed cell death) are malfunctioning. Here, cells can proliferate and grow in an uncontrolled and disorganized manner. Risk factors promoting breast cancer are among others a lack of physical exercise, drinking alcohol, hormone replacement therapy during menopause and childlessness, family history of breast or ovarian cancer. Of major importance are further mutations in the BRCA1 (Breast cancer antigen 1) and BRCA2 (Breast cancer antigen 2) genes, which are known as the “breast cancer susceptibility proteins” (to a certain extent also the p53 gene), which are responsible for 5–10 % of all breast cancer incidents reported and mainly account for breast cancer in young women [40]. These genes are common in mammal species, hence are not of oncogenic nature, but instead function as tumor suppressors within the healthy body [41]. BRCA1 and BRCA2 are part of a complex-group that repairs double-strand breaks in the DNA double helix [42]. Women with a mutated BRCA1/2 gene have a malfunctioning/disabled DNA repair system rendering them exposed to an 80 % risk of developing life-time breast and ovarian cancer, depending on the generation on mutating cells.

Most commonly breast cancer originates from cells of the mammary gland, namely ductal and lobular carcinomas. In early or pre-cancerous stages, abnormal cell proliferation is per definition confined to the inner compartments of the ducts and lobules and carcinomas are labelled as “in-situ” (Fig. 2.8b). Although, in-situ indications are considered rather harmless if remaining in their constitution, since patients usually do not develop distant metastases, they yield a high life-time risk of becoming “invasive carcinomas”, i.e. bursting the basal membrane and infiltrating surrounding tissue. Development of invasive behaviour is of high diagnostic importance, considering destruction of healthy tissue but also potential dissemination and metastasis formation of cancer cells in the lymph nodes, bones, liver, lung and brain. While an early detection of ductal carcinomas in-situ is hence desirable in young patients, a potential over-diagnosis and treatment of the latter in the case of elderly patient is currently under discussion [43]. This is due to the fact that the development from in-situ into invasive carcinomas may last up to 10 years and older women will not benefit from therapy considering the overall survival. In addition to more than 18 malignant tumor histological types and sub-types also benign changes are found in the female breast such as (fibro-)cystic lumps. The most common mass found in young, adolescent woman are benign fibroadenomas which grow in the terminal duct lobular units of the breast [44]. However, benign changes routinely require little action and excision is only indicated in the case of rapid growth or patient discomfort.

The treatment and prognosis of breast cancer is versatile and heavily depends on the specific tumor characteristics. Breast cancer diagnosis has a complementary structure: a physical examination is followed by two-field mammography, ultrasound and in certain indications contrast-enhanced MRI. In rare case, e.g. if a dissemination and metastasis formation of the tumor are suspected, an examination with 18F-Fluorodeoxyglucose Positron Emission Tomography may be indicated [45]. In Germany, a biennial screening mammography is recommended for women aged 50–79 (for more details see Chap. 5). The “Breast Imaging Reporting and Data System” (BIRADS), which is the standard risk assessment and quality assurance tool in breast diagnostics, classifies mammographic findings into BIRADS I–VI categories [35].

BIRADS classification (ACR)

- I —negative finding, i.e. no architectural disorder, abnormalities or suspicious microcalcifications are present in the mammogram.
- II —benign finding, including fibroadenomas, oil cysts, lipomas and galactoceles.
- III —Probably benign finding with a low malignancy risk of $\leq 2\%$.
- IV —Suspicious finding with an intermediate malignancy risk of 2–95 %.
- V —Highly suspicious finding with a high malignancy risk of $\geq 95\%$.
- VI —Histopathologically verified carcinoma.

In the case of a III–V finding, a core or vacuum-assisted biopsy of the suspicious mass is taken under local anaesthesia (guided by mammography or ultrasound) and histopathological work-up is performed. The classification of tumors is complex and comprises a multi-layered assessment. Histologically, different tumor types are defined according to the WHO classification depending from the tissue type they originate from: the most frequent histological type is the invasive ductal carcinoma, not otherwise specified (NST), accounting for 70 % of all invasive breast cancers. Less common types are among others the invasive lobular carcinoma, tubular, medullary and mucinous carcinoma [46]. Grading further compares to what extent cancer cells and their core are still differentiated in comparison to healthy cells (well differentiated—low grade, moderately differentiated—intermediate grade, and poorly differentiated—high grade). Breast cancer staging according to the TNM system describes macroscopical properties of the tumor within the breast, including tumor size (T), a potential invasion of the axillary lymph nodes in the armpits (N), and whether the tumor exhibits a metastatic behaviour (M) [47]. Besides, also a description of the tumor cells with respect to their biochemical entities (Receptor status, DNA assays) is available.

Breast cancer therapy is increasingly individualized depending on tumor type and biology, size, nodal state, distant metastases as well as age of the patient. Nevertheless, the standard therapy of breast cancer is the surgical removal of the lesions and, if indicated, an adjuvant or neoadjuvant medication with cytostatica. Although also affecting healthy cells, cytostatica predominately destroy cancerous cells, which

yield a strongly increased self-replication rate. After surgery, radiotherapy may be applied to the surrounding soft-tissue as well as the adjacent lymph nodes with the goal of destroying spread tumor cells and preventing a recurrence of the tumor [48]. In tumors expressing hormonal receptors and/or growth factor receptors, antihormonal and/or antibody therapy is recommended, in which tumor cells are deprived of their basis of cell growth via blocking the production of oestrogen and growth factors.

References

1. Als-Nielsen, J., & McMorrow, D. (2011). *Elements of modern X-ray physics*. Hoboken: Wiley.
2. Willmott, P. (2011). *An introduction to synchrotron radiation: Techniques and applications*. Chichester: Wiley.
3. Paganin, D. (2006). *Coherent X-Ray optics*. Oxford: Oxford University Press.
4. Sanchez del Rio, M., & Dejus, R. (2011). XOP v2.4: recent developments of the X-ray optics software toolkit. *Proceedings of SPIE*, 8141, 814115.
5. Wang, Y. (2007). Intuitive dimensional analyses of the energy and atomic number dependences of the cross sections for radiation interaction with matter. *Journal of X-Ray Science and Technology*, 15, 169–175.
6. Klein, O., & Nishina, Y. (1929). Über die Streuung von Strahlung durch freie Elektronen nach der neuen relativistischen Quantendynamik von Dirac. *Zeitschrift für Physik*, 52, 853–869.
7. Thüring, T., Abis, M., Wang, Z., David, C., & Stampanoni, M. (2014). X-ray phase-contrast imaging at 100 keV on a conventional source. *Scientific Reports*, 4, 5198.
8. Talbot, H. (1836). Facts relating to optical science. *Philosophical Magazine* IV, 9.
9. Edgar, R. (1969). The Fresnel diffraction images of periodic structures. *Optica Acta*, 16, 281–287.
10. Saleh, B., & Teich, M. (2007). *Fundamentals of photonics*. Hoboken: Wiley-Interscience.
11. Guigay, J., et al. (1971). On Fresnel diffraction by one-dimensional periodic objects, with application to structure determination of phase objects. *Optica Acta*, 18, 677–682.
12. Arrizon, V., & Ojeda-Castaneda, J. (1994). Multilevel phase gratings for array illuminators. *Applied Optics*, 33, 5925–5931.
13. Weitkamp, T., David, C., Kottler, C., Bunk, O., & Pfeiffer, F. (2006). Tomography with grating interferometers at low-brilliance sources. *Proceedings of SPIE*, 6318, 63180.
14. Suleski, T. (1997). Generation of Lohmann images from binary-phase Talbot array illuminators. *Applied Optics*, 36, 4686–4691.
15. Xin, L., Jin-Chuan, G., Xiang, P., & Han-Ben, N. (2007). Visibility in differential phase-contrast imaging with partial coherence source. *Chinese Physics*, 16, 1632.
16. Hipp, A., et al. (2014). Energy-resolved visibility analysis of grating interferometers operated at polychromatic X-ray sources. *Optics Express*, 22, 30394–30409.
17. Momose, A. (2003). Phase-sensitive imaging and phase tomography using X-ray interferometers. *Optics Express*, 11, 2303–2314.
18. Wen, H., et al. (2013). Subnanoradian X-ray phase-contrast imaging using a far-field interferometer of nanometric phase gratings. *Nature Communications*, 4, 2659.
19. Takeda, Y., et al. (2007). X-Ray phase imaging with single phase grating. *Japanese Journal of Applied Physics*, 46, 89–91.
20. Momose, A., et al. (2003). Demonstration of X-Ray Talbot interferometry. *Japanese Journal of Applied Physics*, 42, 866–868.
21. Weitkamp, T., et al. (2005). X-ray phase imaging with a grating interferometer. *Optics Express*, 13, 6296–6304.

22. David, C., et al. (2007). Fabrication of diffraction gratings for hard X-ray phase contrast imaging. *Microelectronic Engineering*, 84, 1172–1177.
23. Bech, M. (2009). *X-ray imaging with a grating interferometer*. Copenhagen: University of Copenhagen.
24. Pfeiffer, F., et al. (2008). Hard-X-ray dark-field imaging using a grating interferometer. *Nature Materials*, 7, 134–137.
25. Malecki, A., Potdevin, G., & Pfeiffer, F. (2012). Quantitative wave-optical numerical analysis of the dark-field signal in grating-based X-ray interferometry. *Europhysics Letters*, 99, 48001.
26. Bech, M., et al. (2010). Quantitative X-ray dark-field computed tomography. *Physics in Medicine and Biology*, 55, 5529.
27. Strobl, M. (2014). General solution for quantitative dark-field contrast imaging with grating interferometers. *Scientific Reports*, 4, 7243.
28. Yashiro, W., Terui, Y., Kawabata, K., & Momose, A. (2010). On the origin of visibility contrast in X-ray Talbot interferometry. *Optics Express*, 18, 16890–16901.
29. Köhler, T., Jürgen Engel, K., & Roessl, E. (2011). Noise properties of grating-based X-ray phase contrast computed tomography. *Medical Physics*, 38, 106.
30. Born, M., & Wolf, E. (1999). *Principles of optics—electromagnetic theory of propagation, interference and diffraction of light*. Cambridge: Cambridge University Press.
31. Pfeiffer, F., Weitkamp, T., Bunk, O., & David, C. (2006). Phase retrieval and differential phase-contrast imaging with low-brilliance X-ray sources. *Nature Physics*, 2, 258–261.
32. Engelhardt, M., et al. (2008). The fractional talbot effect in differential X-ray phase-contrast imaging for extended and polychromatic X-ray sources. *Journal of Microscopy*, 232, 145–157.
33. Thuering, T., et al. (2011). High resolution, large field of view X-ray differential phase contrast imaging on a compact setup. *Applied Physics Letters*, 99, 041111.
34. Kopans, D. (2006). *Breast imaging*. Baltimore: Lippincott Williams & Wilkins.
35. D’Orsi, C., et al. (2013). *ACR BIRADS atlas, breast imaging reporting and data system*. Preston: American College of Radiology.
36. Lynch, J. (2007). The Breast: cross section scheme of the mammary gland. http://en.wikipedia.org/wiki/File:Breast_anatomy_normal_scheme.png.
37. McCormack, V., & Silva, I. (2006). Breast density and parenchymal patterns as markers of breast cancer risk: A meta-analysis. *Cancer Epidemiology, Biomarkers and Prevention*, 15, 1159–1169.
38. World cancer report (2008). (International Agency for Research on Cancer, Lyon, 2008)
39. Coleman, M., et al. (2008). Cancer survival in five continents: A worldwide population-based study. *The Lancet Oncology*, 9, 730–756.
40. Campeau, P., Foulkes, W., & Tischkowitz, M. (2008). Hereditary breast cancer: New genetic developments, new therapeutic avenues. *Human Genetics*, 124, 31–42.
41. Duncan, J., Reeves, J., & Cooke, T. (1998). BRCA1 and BRCA2 proteins: Roles in health and disease. *Molecular Pathology*, 51, 237–247.
42. Friedenson, B. (2007). The BRCA1/2 pathway prevents hematologic cancers in addition to breast and ovarian cancers. *BMC Cancer*, 7, 152–162.
43. Kumar, A., Bhatia, V., & Henderson, I. (2005). Overdiagnosis and overtreatment of breast cancer: Rates of ductal carcinoma in situ: A US perspective. *Breast Cancer Research*, 7, 271–275.
44. Jayasinghe, J., & Simmons, P. (2009). Fibroadenomas in adolescence. *Current Opinion in Obstetrics and Gynecology*, 21, 402–406.
45. Bellon, J., et al. (2004). Evaluation of the internal mammary lymph nodes by FDG-PET in locally advanced breast cancer. *American Journal of Clinical Oncology*, 27, 407–410.
46. Mammakarzinom der Frau: Diagnostik, Therapie und Nachsorge – S3 Leitlinie Mammakarzinom. (AWMF, 2012).
47. Denoix, P. (1946). Enquete permanent dans les centres anticancereaux. *Bulletin - Institut National d’Hygiene*, 1, 70–75.
48. Massarut, S., et al. (2006). Intraoperative radiotherapy impairs breast cancer cell motility induced by surgical wound fluid. *Journal of Clinical Oncology*, 24, 10611.

Grating-Based X-Ray Phase-Contrast Mammography

Scherer, K.H.

2016, XX, 140 p. 47 illus., 33 illus. in color., Hardcover

ISBN: 978-3-319-39536-4